Communication

Wide Scan, Active K-Band, Direct-Integrated Phased Array for Efficient High-Power Tx-Generation

Ahmad Emadeddin and B. L. G. Jonsson

Abstract— **In this communication, we propose a new wide-scan active direct-integrated 1 × 5 phased array antenna (AIPAA) for mm-Wave applications. The AIPAA's unit-cell comprises three K-band miniaturized tapered slot elements, a GaN high electron mobility transistor (HEMT) as a power amplifier (PA), a stability circuit, an input matching network (M.N.), and biasing components. The tapered slot antenna element is reshaped so that its input impedance closely matches the optimal load impedance of the HEMT ($Z_{opt} = 6 + j38\ \Omega$ at 22 GHz), which enhances the system efficiency. The peak-integrated PAs' power-added efficiency (PAE_p) is ≥56% with ≤9% variation over scan coverage (±50°) at 1.5 dB power backoff from P1dB. The peak AIPAA system power-added efficiency (PAE_s) is 51% with a peak array radiation efficiency of 92%. The relative frequency bandwidth with PAE_p above 25% is between 9% and 13% over the scan range. The proposed AIPAA demonstrates less than 0.9 and 1 dB scanloss over the scan coverage in terms of antenna array gain and PAs' power gain (G_p), respectively. The peak PA-integrated array gain and EIRP at P1dB of 24 dBi and 51 dBm are achieved, respectively. The proposed AIPAA's size is $18 \times 58 \times 17\ mm^3$ with a cell of $9.2 \times 6.5 \times 1.8\ mm^3$. The measurements are in good agreement with electromagnetic and circuit co-simulation results.**

Index Terms— **Active integrated phased array antenna, beam steering, direct integration, mm-Wave antenna.**

I. INTRODUCTION

Communication on mm-Wave frequencies is currently under development to improve the capacity of the systems in a cost and energy-efficient way. Advanced antenna systems have been proposed for mm-Wave communications to significantly enhance the network performance [1]. The radio front-end of an advanced antenna system is often composed of a phased array antenna together with amplifiers and other hardware to achieve steerability, high efficiency, and time adaptivity. To improve the system efficiency in such a radio front-end, there are efforts to integrate power amplifiers (PAs) with the phased array antenna. This approach is called active integrated phased array antenna (AIPAA) [2], [3]. In mm-Wave applications, such as the high-band 5G and target tracking, wide scan angles coverage is required for a narrow frequency bandwidth together with high-energy efficiency, small size, and cost [4]. In this communication, we propose a new wide scan direct-integrated phased array antenna for Tx mm-Wave applications well suited for advanced antenna systems.

In phased array antennas, both the gain and active reflection coefficients depend on the scan angles due to the mutual coupling between the elements [5], [6]. For efforts to reduce the gain and active reflection variations see [7], [8], [9], [10]. As a novelty of this communication, we advance the array element design of [10]
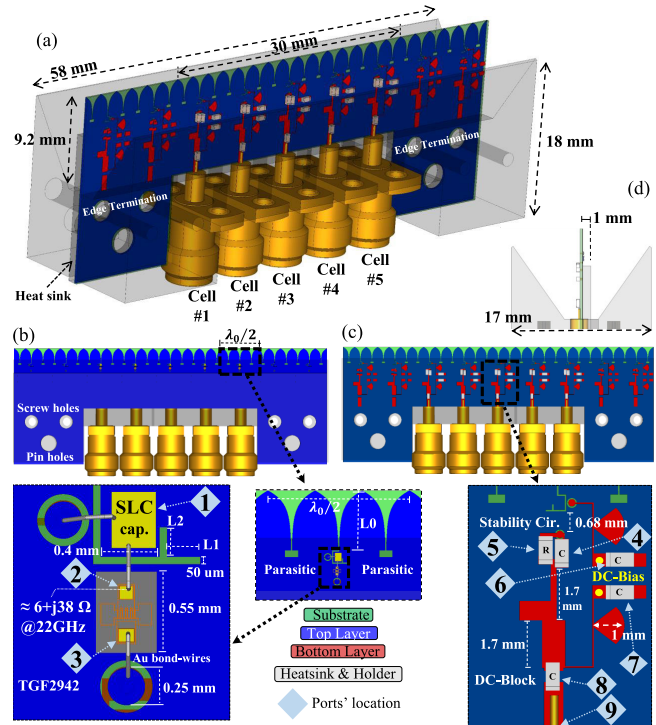
Fig. 1. AIPAA configuration. (a) Perspective view. (b) Front view with its two zoomed-in views indicated by black dotted arrows. (c) Back view with its zoomed-in view indicated by black dotted arrows. (d) Side view. Top layer (blue) and bottom layer (red) of the substrate (green) are connected through a few vias for RF and dc transition. Rhombus: location of a cell's ports.

to be matched closely to the optimum PA load impedance over the frequency band and scan coverage by reshaping and tuning, e.g., the termination of the feed line of the tapered slot antenna. Thus, no intermediate impedance matching components are needed. The design's result demonstrates a considerable improvement in terms of antenna-gain reduction together with a small variation of the active input impedance over the scan range.

The majority of integration between antennas and their active components utilize a 50 Ω interface with a matching network (M.N.), see, e.g., [2], [11]. For mm-Waves, such M.N. tends to cause problems due to the physical size and undesired radiation in addition to their insertion loss [12]. To counter these undesirable effects, a *direct integration* between the active components and the array elements has been proposed [13]. This increases the demands on the antenna design, based on the given off-the-shelf active components. It is a careful examination and a method development of direct integration through antenna tuning that is one of the main focus and result of the communication.

Below follows a short review of directly integrated antennas and arrays. A directly integrated transmitter antenna structure at 5.5 GHz
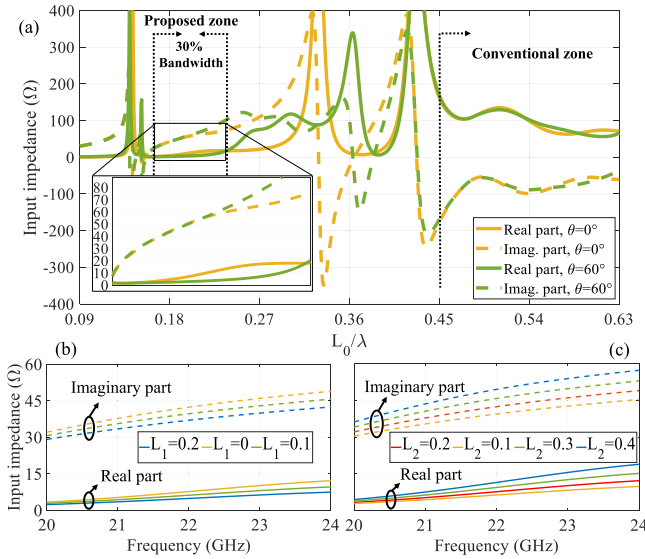
Fig. 2. (a) Tapered slot impedance behavior (unit-cell) as a function of electrical length, L_0/λ [see Fig. 1(b)], for the broadside and 60° scan. (b) Tuning L_1 (mm) while $L_2 = 0.1$ mm at broadside [Fig. 1(b)]. (c) Tuning L_2 (mm) while $L_1 = 0.1$ mm at broadside.

with a 3.5% PAE improvement was proposed in [13]. In [14], a K-band slot antenna element with direct-integrated GaN PA and a total efficiency of 40% was presented. Both [13], [14] examine the active integrated antennas (AIAs) as isolated elements.

A 16-element directly integrated X-band array was proposed in [15] with an EIRP of 10 W at 26% efficiency for the broadside beam. Other active array concepts with beam-steering capabilities are presented in [16], [17], [18], [19], [20], and [21]. In [19], an integrated design was introduced for a 1-D active array with 30° scan capability and peak efficiency of 21%. An array with peak efficiency of 21.5% for ±26° scan coverage at 44 GHz was proposed in [21]. In [22], an approach for designing an AIPAA, whose unit-cell showed a 47% peak drain efficiency with ±60° E-plane and ±37° H-plane coverage, was presented. In [23], an active integrated array element with PA MMIC via on-chip structure was introduced with a peak PAE of 40%, a bandwidth of 11.3% (PAE ≥ 20%), and a 2-D coverage of ±55° and ±40°.

In this communication, we propose a direct-integrated 1×5 K-band AIPAA representing substantial improvement in terms of a wider bandwidth with higher PAE over a wide scan coverage for all cells of the finite AIPAA (not an unit-cell). In addition to utilizing the off-the-shelf active components, the proposed design method considers the simultaneous excitation, all coupling, and edge effects which widens the usability of the approach. The proposed structure, depicted in Fig. 1, consists of one RO4003-substrate layer, with a 0.3 mm thickness, which makes it straightforward to implement and integrate compared with multilayer AIA.

II. DESIGN METHOD

In this section, we describe the design of the PA. A compliance-level method is proposed below to match nonstandard-impedance antenna elements so that the overall PAE remains high. The second part of this section describes the design of an antenna element that is directly integrated with the PA. This communication concerns a transmitting array, and hence the focus is on PAs.

A. Power Amplifier

This section focuses on the PA and to develop a compliance-level method to guarantee the desired overall PAE. In this design, we follow

the requirements represented in [24]: PAE ≥ 25%, a frequency bandwidth 5%–10%, and output power $P_{out} \geq 25$ dBm, centered around 22 GHz.

The methodology of designing different classes of a PA is well described in, e.g., [25]. The considered 2 W discrete GaN high-electron mobility transistor (HEMT) RF die-transistor TGF2942, manufactured by Qorvo, is designed in class AB with a $V_{drain} = 20$ V supply and $V_{gate} = -2.8$ V which results in $I_{DQ} = 20$ mA. The transistor is modeled with the Modelithics Qorvo GaN large-signal library in Advance Design System (ADS) software. It is worth noting that the HEMT transistor is not unconditionally stable. Therefore, a stability circuit is designed to make it unconditionally stable. A load-pull simulation for maximum PAE on TGF2942 along with its input circuits, Fig. 1(c), results in the optimum PA load impedances and the corresponding PAE circles over the intended frequency band. The load impedance is $Z_{opt} = 6 + j38$ Ω at 1.5 dB power backoff from P1dB and 22 GHz. The maximum PAE of the TGF2942 occurred at around P1dB is ≈58% at 22 GHz.

The PAE circles are transferred to the center of Smith chart. This is equivalent to choosing the conjugate of the optimum PA load impedance as the internal impedance for the power wave reflection coefficient [26]. So, each impedance point on the PAE-circle with PAE = 25%, corresponds to a reflection coefficient with respect to Z_{opt}^*. The minimum value is defined as *the compliance-level, $\Gamma_{C.L.}$*, e.g.,

$$\Gamma_{C.L.}(f, P_{in}) = \min_{Z_{PAE=25\%}} \left| \frac{Z_{PAE=25\%} - Z_{opt}}{Z_{PAE=25\%} + Z_{opt}^*} \right| \qquad (1)$$

where f denotes the frequency. The array antenna will be the load of the PA. Therefore, the worst active reflection coefficient of the array elements with Z_{opt}^* as port impedance (internal impedance) should be less than the $\Gamma_{C.L.}$ to guarantee an overall efficiency of PAE ≥ 25% in the PAs.

B. Antenna Element and Integration

An array-element design has several constraining parameters apart from the input impedance, such as its far-field radiation pattern, mutual coupling to neighboring elements, and scanability. To direct-integrate a PA with the array, the input impedance of the array elements needs to be matched without an intermediate M.N. to the above-discussed Z_{opt}, see Section II-A. We propose to utilize the physical behavior of small radiators (miniaturized antenna) together with a reshaping, e.g., adding parasitic elements and feeding reshaping, to solve the matching requirement to PA optimum impedance. Small antennas tend to have a small real-part impedance and nominally large reactance [27].

The basic element in our investigation is a tapered slot element fed by a bond wire. The antenna ports are placed at the drain pad (port 2) of the transistors, see Fig. 1(b). Fig. 2(a) depicts its unit-cell input impedance behavior as a function of its electrical length, L_0/λ, see Fig. 1(b), both at broadside, $\theta = 0°$ and 60° scan angle. Observe that it provides a small input resistance at around $L_0 = 0.2\lambda$. This size provides an input impedance of $6 + j50$ Ω at 22 GHz with a broadside bandwidth of 30% reducing at ±60° scanning, Fig. 2(a).

The phased array antenna design approach of [10] is employed to design a wide scan coverage AIPAA. The AIPAA's unit cell includes two unloaded similar-sized parasitic-tapered slot elements enclosing the excited element, see Fig. 1(b). The size of the excited tapered slot element is $0.2 \times 0.16 \times 0.02\lambda^3$ at 22 GHz.

The local shape of the feeding region is used to fine-tune the integration. The integration technique, depicted in Fig. 1(b), results in a higher degree of integration in which the PA couples directly
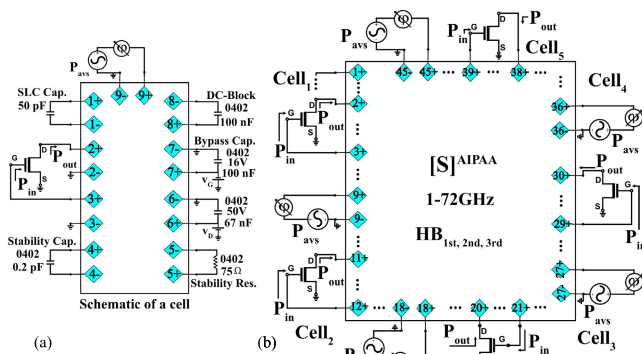
Fig. 3. EM/circuit co-simulation schematic from 1 to 72 GHz. The schematic drawing of (a) sample cell modeled with nine differential ports and (b) AIPAA with 45 differential ports.

Fig. 4. Radiation pattern characterization of the AIPAA. Yellow color: EEP for center cell. Orange color: Peak-envelop of the scanned beams with 3° scan resolution and the array gain, $G_{Ant.}$, variation from 13.4 to 12.5 dBi. Dash lines: beam steering at $0°$, $20°$, $30°$, and $50°$.

to the tapered slot through a bond wire across a narrow slot line in the feeding region. The bonding technique is the wedge-wedge with 25 μm diameter gold wires, e.g., implemented with loop formation and a constant wire length of 372 μm resulting in the height of $\sim$80 μm for exciting the tapered slot antennas (placement from the drain pad to SLC capacitor). The other two bond-wires, located at the gate and the SLC capacitor, have a length of $\sim$445 μm. The dc-biasing bondwire, which is located at the SLC capacitor toward the circular pad, is designed to exhibit a high impedance (open circuit) at RF frequencies over the intended frequency bandwidth. The SLC capacitor, works as a dc-block, is placed to provide isolation between the RF lines and the bias voltages/GND. The width of the SLC capacitor limits the minimum length of the narrow slot line, see Fig. 1. The L-shaped stubs, L_1 and L_2, at the end of the narrow slot line, are fine-tuned ($L_1 = 0.15$ mm and $L_2 = 0.1$ mm) to approach the optimum PA impedance over the operating bandwidth, see Fig. 2(b) and (c).

The introduced $\Gamma_{C.L.}$ (1) is compared with the active reflection coefficients over different scan angles and frequencies. Wherever the absolute value of the active reflection coefficients for each element is below the $\Gamma_{C.L.}$, this corresponds to that the PA's PAE (PAE_p) performance is better than the PAE-level associated with $\Gamma_{C.L.}$. Furthermore, wherever the active reflection coefficients level is below the $\Gamma_{C.L.}$ with a margin of ≤ -10 dB, this corresponds to excellent performance with respect to the Z_{opt}^* meaning the PAE_p performance is close to the expected maximum PAE.

Thus, the method of defining a frequency-dependent compliance level at a given PAE-level provides a practical and efficient reference, which is used to design/adjust the array antenna with respect to the optimal PA output impedance. The approach guarantees the desired overall performance over the considered frequency bandwidth and scan coverage. Note that the design also aims for high load reflection coefficients of the second and third harmonic [28], [29] during the geometry shaping/tuning process.

III. ACTIVE INTEGRATED PHASED ARRAY

This section focuses on the final array design, its co-simulation, and the system performance as a function of frequency and scan range. The analysis with K-connectors, a holder, and a heatsink is done for a finite 1×5 AIPAA.

A. Co-Simulation Technique

Every active integrated system consists of both a linear passive part and an active part. A combined EM and circuit co-simulation (below denoted with co-simulation) is required to characterize the behavior of such systems. Here we have used a combination of the CST studio suite and the harmonic balance (HB) simulation in the ADS
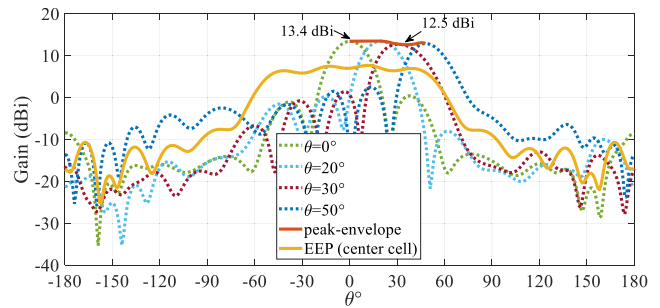
software package. The passive parts of the system are simulated in CST, utilizing the full-wave electromagnetic 3-D simulation. This determines the scattering matrix which is then used to evaluate the overall system performance in ADS.

Each AIPAA's cell is modeled with the following nine differential ports: input RF connector (9), PA drain (2), PA gate (3), drain bias terminal (6), gate bias terminal (7), two stability circuit components (4,5), in/out dc-blocks (1,8), see Figs. 1(b) and (c) and 3(a). Hence, to simulate the finite 1×5 AIPAA, there are 45 ($= 5 \times 9$) differential ports in its 3-D full-wave simulation, Fig. 3(b).

The scattering matrix is stored as a touchstone file over a frequency span from 1 to 72 GHz. The reason for such a wide bandwidth is to account for instabilities and harmonic behaviors both at the lower frequencies and the higher frequencies (three harmonic tones). Recall that the operating frequency is 20–24 GHz. The touchstone file is used in the ADS HB simulator to analyze the small- and large-signal behavior with three harmonics tones. All coupling effects and the scanning behavior are automatically included for the finite AIPAA by a proper phase distribution between the excitation signals. Thus, all small- and large-signal parameters are evaluated as a function of frequency and scan angles by the co-simulation technique. The investigated properties include power gain, PAE, harmonics' power, array beam steering patterns, and the scattering matrix.

Thus, the AIPAA design and simulation approach is separated into three steps: PA design and extracting the Z_{opt} and the $\Gamma_{C.L.}$ (HB simulator), antenna design with respect to the Z_{opt}^* and the $\Gamma_{C.L.}$ (CST full-wave), and the touchstone-interconnection technique of the whole structure with the scattering matrix of the full 1×5 antenna array in wide bandwidth and scan range (co-simulation HB simulator).

B. 1×5 AIPAA

The AIPAA structure with heat-sink, two-sections holder, screws' position, and pins' place are depicted in Fig. 1. To reduce the edge effect of the array, the array is extended with two additional parasitic cells on each side of the array.

A steady-state thermal analysis is applied on the 1×5 AIPAA with heatsink by CST thermal solver. Its maximum steady-state temperature is $\sim$73 °C which conforms to the safe operating temperature of the HEMT in its datasheet. The maximum temperature of $\sim$40 °C was measured on the manufactured AIPAA when cell 2 was excited. The heat sink is a thin aluminum sheet with a thickness of 1 mm to transfer the heat to the holder. Its position is chosen to be on the top layer of the substrate, see Fig. 1(d). The up/down asymmetry, caused by the heat sink, weakly impacts on the radiation pattern in H-plane whose -10 dB beamwidth is from $87°$ to $-89°$.

Using the parasitic elements results in an antenna-gain reduction of only 0.9 dB with the peak array gain, $G_{Ant.}$, of 13.4 dBi over the
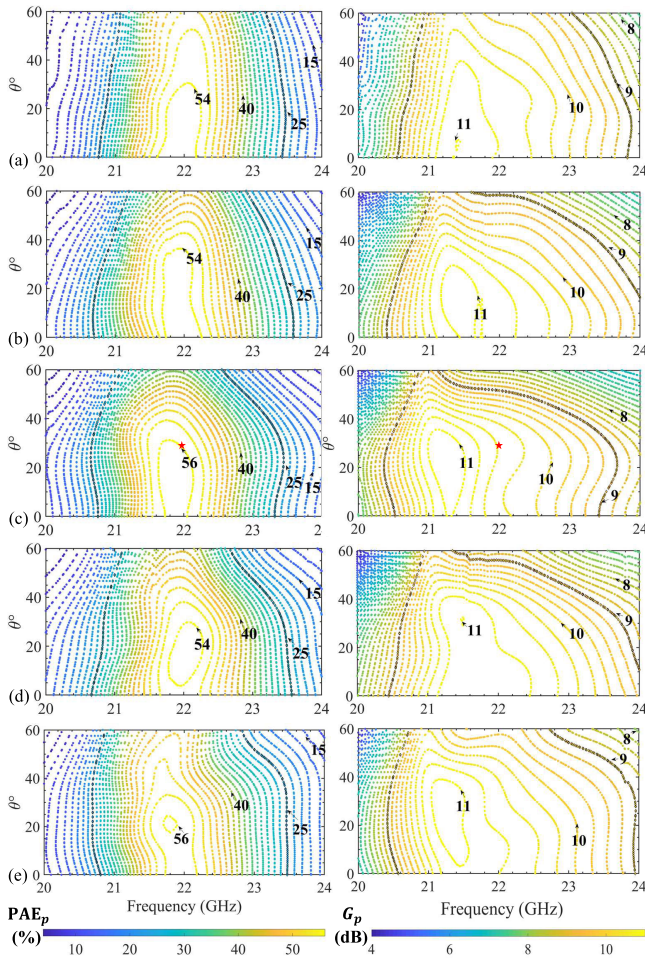
Fig. 5. PAE_p and G_p performance as a function of frequency and scan range ($\theta \in [0, 60]$) for all simultaneously excited 1×5 AIPAA cells at $P_{in} = 20$ dBm (1.5 dB backoff from P1dB) (a) cell 1, (b) cell 2, (c) cell 3 (center cell), red star: calculation point of the peak PAE_s, (d) cell 4, and (e) cell 5.

scan range $\pm 50°$, see Fig. 4. Note that for this figure the antenna ports are placed at the drain pads (port2), see Fig. 1(b), with Z^*_{opt} as their impedance. The embedded radiation pattern (EEP), for the center element (yellow) and the peak envelop of the scanned beams with 3° scan resolution (orange) are depicted in Fig. 4 at 22 GHz. The small discrepancy between the shape of the peak envelope and the center cell's EEP is due to the edge effects. Due to E-plane symmetry, scan to $[-50°, 0°]$ behaves identically. The peak array radiation efficiency, including the bond wire losses, is 92% and always $\geq 86\%$ over the scan coverage.

In this AIPAA design technique, the PAs' drain power (P_{out}) and gate power (P_{in}) for all cells are available as a function of frequency, scan range (θ), dc-power (P_{dc}), and input power level (P_{avs}), see Fig. 3. Therefore, the PAs' PAE (PAE_p) and power gain (G_p), for all simultaneously excited cells, are calculated from ($P_{out} - P_{in}$)/P_{dc} to evaluate the design technique. The PAE_p and G_p are plotted in Fig. 5 as a function of frequency and scan range (θ) at $P_{in} = 20$ dBm (1.5 dB backoff from P1dB) for all cells. The results are reported $\theta \in [0, 60]$ degrees due to the E-plane symmetry. Note that the aggregate PAE_p performance demonstrates a maximum PAE_p from 47% to 56% over the scan range $\pm 50°$ at $P_{in} = 20$ dBm, Fig. 5 (left column). The relative frequency bandwidth with PAE_p above 25%, highlighted in Fig. 5 (left column), is between 9% and 13% over the scan coverage for all cells. Observe that the peak of G_p is 11 dB for all cells with less than 1 dB variation over the scan range, Fig. 5
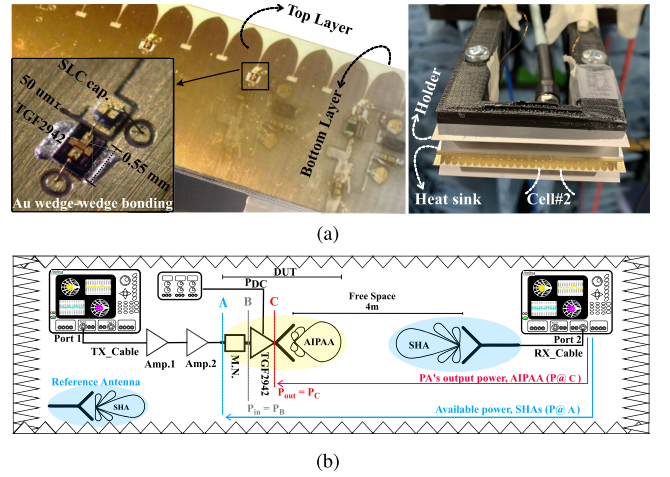

(a)

(b)

Fig. 6. (a) Manufactured AIPAA. The top layer and substrate are translucent to see the bottom layer components. Cell 2 is measured. (b) Measurement setup in an anechoic chamber in which P_B and P_C represent P_{in} and P_{out} of PA, respectively.

(right column). In the figures, the 9 dB contour is also highlighted to show the relative frequency bandwidth of 8%–15% for 2 dB-G_p variation and $\geq 12\%$ for 3 dB-G_p variation over the scan range for all cells. The maximum AIPAA's PA-integrated gain, including the G_p and the array gain, is 24 dBi. It is worth noting that at P1dB the output power of each PA is $P_{out} = 31$ dBm per cell meaning the AIPAA's EIRP of 51 dBm.

The PAs' output power (P_{out}) is exactly the same as the accepted power of the array antenna elements, Figs. 3(b) and 1(b). Thus, the AIPAA system power-added efficiency (PAE_s) with respect to the total radiated power per each cell is related to its corresponding PAE_p through the relation

$$PAE_s = PAE_p \left(1 - \frac{G_p}{G_p - 1}(1 - \eta_{rad.}) \right). \quad (2)$$

The element radiation efficiency of each cell ($\eta_{rad.}$) is approximated by the array radiation efficiency which was reported over the scan range and frequency bandwidth. The peak PAE_s of 51% occurs at the red star point depicted in Fig. 5(c) with $G_p = 10.5$ dB, $PAE_p = 56\%$, and $\eta_{rad.} = 92\%$. The relative frequency bandwidth with PAE_s above 22% is between 8.5% and 13% over the scan coverage for all cells.

IV. EXPERIMENTAL RESULTS AND DISCUSSION

In an AIPAA, a traditional array antenna validation procedure is not possible. To obtain the prototype validation for the AIPAA, we settle for validating certain information through measurements, supplemented with simulated results of the input M.N. insertion loss and the antenna element gain. The parameters that we aim for are some far-field information, G_p, and PAE_p. The experimental setup utilizes the open-circuit measurement similar to [30]. Cell 2 is chosen as the focus port for measurements to investigate the agreement for an asymmetry case. The manufactured prototype is depicted in Fig. 6(a).

A schematic sketch of the measurement setup is depicted in Fig. 6(b), introducing the reference planes A-C. All measurements are conducted in an anechoic chamber. A digital dc-power supply is connected to the AIPAA to log its power consumption. The Anritsu MS4647B vector network analyzer (VNA) is connected to two pre-amplifiers, to drive the AIPAA to input power levels up to 24 dBm. The receiving antenna is a standard horn antenna (SHA), which is connected to the VNA-port nr. 2, see Fig. 6(b).

The characterization process consists of both measurement steps and post-processing. The measurement sweeps are repeated 100 times
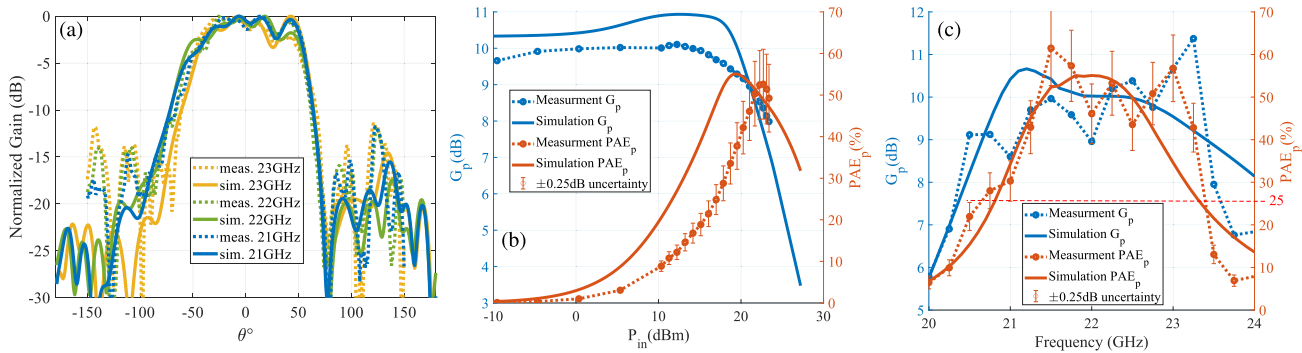
Fig. 7. Measured and simulated results of the AIPAA by excitation at cell 2 while leaving the other ports open. (a) Normalized open-circuit active-EEP. (b) Power Gain (G_p) & PAE_p versus P_{in} [=P_B in Fig. 6(b)] at 22 GHz, and (c) versus frequency at P1dB [Fig. 7(b)] with a measurement uncertainty of ±0.25 dB.

for each step to reduce random errors. Note that in all measurements, the VNA is calibrated for each measurement round of gains, losses, and received powers. An unratioed trace on the VNA receiver (VNA-port nr. 2) is employed to measure the accurate absolute power level, calibrated for power accuracy by an Anritsu USB power sensor (MA24340A).

In the measurement setup with the SHA, bottom left corner in Fig. 6(b), mounted as the device under test (DUT) at reference plane A, the received power at VNA-port nr. 2 is measured. Note that the path from reference plane A toward VNA-port nr. 2 is passive in this step. Furthermore, the following quantities are known from their measurement data: the gain of the SHA, Rx-cable loss, and the free space loss. The signal power at reference plane A, P_A, can hence be determined experimentally over the measurement (Friis formula), blue arrow in Fig. 6(b). The P_A, which is considered as the available power to the AIPAA, represents the signal power amplified by the pre-amplifiers at the input port of the AIPAA.

In the next setup, the AIPAA is mounted as DUT. In this step, the radiated peak power and radiation pattern are measured. The radiation pattern is measured in the small-signal range (linear region) from $-150°$ to $+150°$, see Fig. 7(a). The peak power is measured both in the small- and large-signal range. The power at the reference plane C, P_C, is determined from the known data of the path from the VNA-port nr. 2 to reference plane C together with simulated antenna gain (Friis formula), see the red arrow in Fig. 6(b). The P_{dc} is also logged for the measurement. The P_C is the PA's output power ($P_{out} = P_C$). But to determine G_p and PAE_p, the PA's input power ($P_{in} = P_B$) is obtained through post-processing by utilizing a co-simulation data of the M.N. insertion loss with the same available powers (P_A) and frequencies as the measurements.

In Fig. 7(a), the normalized measured and simulated open circuit active EEPs in the E-plane are depicted for 21–23 GHz. The agreement in the half-space $\theta \in [-90°, 90°]$ provides a good validation of the far-field behavior. The discrepancy in the other half-space is associated with the scattering effects from the dc-power supplies and other instruments which could not be perfectly shielded. The simulated and measured AIPAA's performance (excitation at cell 2) in terms of G_p and PAE_p are plotted in Fig. 7(b) and (c) as a function of P_{in} and frequency, respectively. The maximum measured G_p is close to 10 dB as a function of input power at 22 GHz [see Fig. 7(b)]. This behavior shows a good agreement with the co-simulation result of ~11 dB. The maximum PAE_p is 52.6%, which is observed at around P2dB in the measurement. This is close to the maximum PAE_p in co-simulation with 55% at P1dB, see Fig. 7(b).

In Fig. 7(c), the frequency dependence of G_p and PAE_p at P1dB are depicted. Note that the measured frequency bandwidth

TABLE I
ACTIVE INTEGRATED ARRAY COMPARISON

Config.	2×2 array[1]	1×5 array[2]	1×2 array[3]	AiUC[4]	proposed AIPAA[5]
f_0 [GHz]; Bandwidth [%] (criteria)	2; 22.6 (PAE≥ 50%)	10; 2 ($S_{11} \leq -10$dB)	5; 2.5 ($S_{11} \leq -10$dB)	20; 4.1 (3dB-G_p)	22; 15 (2dB-G_p) 13 (PAE$_p \geq$ 25%) 13 (PAE$_s \geq$ 22%)
P_{1dB} [dBm]	7	-	-10	21	21.5
Max.G_p [dB]	14	10	11.5	8.4	11
PA-integrate Gain [dBi]	27.5	15.9	18.9	14.2	24
Max.efficiency (type) [%]	65 (PAE)	-	21 (PAE)	47 (drain)	56 (PAE$_p$) 51 (PAE$_s$)
Scan range, Scanloss [dB] @parameter	-	-	@30°, -	±60°, 2.1@G_T	±50°, 1@G_p 0.9@$G_{Ant.}$; ±60°,2.2@G_p
cell size λ_0^2	0.5×0.77	0.8×1.3	0.3×0.8	0.62×0.51	0.67×0.5

[1] PCB + GaAs pHEMT; 50Ω; class E [11].
[2] PCB + AlGaAs pHFET; 50Ω; class A [18].
[3] PCB + HJ-FET; direct imp. match; class A [19].
[4] PCB + metal base + GaN HEMT; direct imp. matching; class AB [22].
[5] PCB + metal heat sink + GaN HEMT; direct imp. matching; class AB.

20.6–23.4 GHz of $PAE_p \geq$ 25% agrees well with the simulated 13% bandwidth. The frequency bandwidth with G_p variation below ±1.2 dB in the measurement and ±1 dB in the simulation starting from G_p = 10 dB are similar.

An A-type standard uncertainty estimation, utilizing the standard deviations of the repeated measurements, is also applied to the measurement results [31]. Apart from the mean value calculation of the 100 times repetition during each measurement, the same measurement procedures are again repeated within a week to determine the standard deviation of the mean values (both SHA and AIPAA as the DUT). In the uncertainty analysis, two error factors are considered: measurement repeatability (ten times) and undesirable scattering effects from other instruments (ten movements in the chamber). A combined standard uncertainty of ±0.25 dB is finally obtained from the measurement data. Other error factors: such as manufacturing, component, and assembly tolerances may be the source of the remaining small discrepancy between measurements and simulations.

Observe that the differences between the system performance in Figs. 5 and 7 stem from that Fig. 5 displays the 1×5 AIPAA with all five ports excited, while Fig. 7 concerns the open circuit conditions on ports 1, 3, 4, 5 and cell 2 excited.

In Table I we compare the system performance of the proposed 1×5 AIPAA with five simultaneous excited ports and the previously reported designs [11], [18], [19], [22]. The proposed AIPAA and [22] utilize the same GaN HEMT device. To summarize the system performances, in addition to the low scanloss, the proposed AIPAA provides both a higher G_p and PAE in a wider frequency bandwidth, 15% for 2 dB-G_p, 13% for both $PAE_p \geq 25\%$ and $PAE_s \geq 22\%$. The performance represents a substantial improvement in comparison with the prior state-of-the-arts.

V. CONCLUSION

Wide scan coverage with high efficiency realized in a cost-effective way is of interest in high-power advanced antenna systems at mm-Wave communication systems. The proposed 1×5 AIPAA offers a wide scan capability ($\pm 50°$) for efficient K-band high-power Tx-applications. The applied direct-integration technique and design approach guarantees the intended system performance over the desired frequency bandwidth and scan coverage. The proposed simultaneously excited AIPAA, considering all coupling and edge effects, demonstrates a peak PAE_p of 56% with a peak PAE_s of 51% at 1.5 dB power backoff from P1dB. The maximum relative frequency bandwidth of 13% for both $PAE_p \geq 25\%$ and $PAE_s \geq 22\%$ is achieved while it is 15% for 2 dB-G_p. The peak PA-integrated array gain is 24 dBi with an EIRP of 51 dBm at P1dB. The presented architecture results in an antenna-gain reduction and power gain reduction of 0.9 and ≤ 1 dB over all scan angles within $\pm 50°$, respectively.

The AIPAA system performance represents a substantial improvement in comparison with the previously reported designs in terms of PAE, bandwidth, and low scanloss over a wide scan coverage at K-band frequencies. The AIPAA is manufactured and its measurement results show a good agreement with the co-simulation. The measurement process is supplemented with simulated results and supported by an uncertainty analysis to increase its confidence.

ACKNOWLEDGMENT

REFERENCES

[1] I. Ahmed et al., "A survey on hybrid beamforming techniques in 5G: Architecture and system model perspectives," *IEEE Commun. Surveys Tuts.*, vol. 20, no. 4, pp. 3060–3097, 4th Quart., 2018.

[2] Y. Qian and T. Itoh, "Progress in active integrated antennas and their applications," *IEEE Trans. Microw. Theory Techn.*, vol. 46, no. 11, pp. 1891–1900, 1998.

[3] Marianna. V. Ivashina, "Joint design and co-integration of antenna-IC systems," in *Proc. 13th Eur. Conf. Antennas Propag. (EuCAP)*, Mar. 2019, pp. 1–7.

[4] R. J. Mailloux, *Phased Array Antenna Handbook*, 3rd ed. London, U.K.: Artech House, 2017.

[5] S. Edelberg and A. Oliner, "Mutual coupling effects in large antenna arrays II: Compensation effects," *IRE Trans. Antennas Propag.*, vol. 8, no. 4, pp. 360–367, Jul. 1960.

[6] R. C. Hansen, *Phased Array Antennas*. Hoboken, NJ, USA: Wiley, 2009.

[7] C. Liu, S. Xiao, H. Tu, and Z. Ding, "Wide-angle scanning low profile phased array antenna based on a novel magnetic dipole," *IEEE Trans. Antennas Propag.*, vol. 65, no. 3, pp. 1151–1162, Mar. 2017.

[8] G. Yang, J. Li, D. Wei, and R. Xu, "Study on wide-angle scanning linear phased array antenna," *IEEE Trans. Antennas Propag.*, vol. 66, no. 1, pp. 450–455, Jan. 2018.

[9] Y. Cheng, X. Ding, W. Shao, M. Yu, and B. Wang, "2-D planar wide-angle scanning-phased array based on wide-beam elements," *IEEE Antennas Wireless Propag. Lett.*, vol. 16, pp. 876–879, 2017.

[10] A. Emadeddin and B. L. G. Jonsson, "A new unit-cell architecture applied to active wide-angle scanning phased array," in *Proc. 15th Eur. Conf. Antennas Propag. (EuCAP)*, Mar. 2021, pp. 1–4.

[11] Y. Qin, S. Gao, and A. Sambell, "Broadadd high-efficiency circularly polarized active antenna and array for RF front-end application," *IEEE Trans. Microw. Theory Techn.*, vol. 54, no. 7, pp. 2910–2916, Jul. 2006.

[12] A. Emadeddin and B. L. G. Jonsson, "On direct matching and efficiency improvements for integrated array antennas," in *Proc. Int. Conf. Electromagn. Adv. Appl. (ICEAA)*, Sep. 2019, pp. 0408–0411.

[13] H. Kim, I.-J. Yoon, and Y. Joong Yoon, "A novel fully integrated transmitter front-end with high power-added efficiency," *IEEE Trans. Microw. Theory Techn.*, vol. 53, no. 10, pp. 3206–3214, Oct. 2005.

[14] W. Liao, R. Maaskant, T. Emanuelsson, V. Vassilev, O. Iupikov, and M. Ivashina, "A directly matched PA-integrated K-band antenna for efficient mm-wave high-power generation," *IEEE Antennas Wireless Propag. Lett.*, vol. 18, no. 11, pp. 2389–2393, Nov. 2019.

[15] R. A. York and R. C. Compton, "Quasi-optical power combining using mutually synchronized oscillator arrays," *IEEE Trans. Microw. Theory Techn.*, vol. 39, no. 6, pp. 1000–1009, Jun. 1991.

[16] S. Kawasaki, S. Kawai, T. Yamamoto, K. Takei, and H. Seita, "A 5.8GHz-band active integrated phased array antenna with wireless communication and power transmission functions for space and satellite use," in *Proc. China-Japan Joint Microw. Conf.*, Sep. 2008, pp. 435–438.

[17] J. A. Ortiz et al., "Ultra-compact universal polarization X-band unit cell for high-performance active phased array radar," in *Proc. IEEE Int. Symp. Phased Array Syst. Technol. (PAST)*, Oct. 2016, pp. 1–5.

[18] C.-H. Tsai, Y. A. Yang, S.-J. Chung, and K. Chang, "A novel amplifying antenna array using patch-antenna couplers-design and measurement," *IEEE Trans. Microw. Theory Techn.*, vol. 50, no. 8, pp. 1919–1926, Aug. 2002.

[19] S. N. Nallandhigal and K. Wu, "Unified and integrated circuit antenna in front end—A proof of concept," *IEEE Trans. Microw. Theory Techn.*, vol. 67, no. 1, pp. 347–364, Jan. 2019.

[20] S. Nikhil N. and K. Wu, "Beam-steered radiation from amplifying active integrated array antenna," in *Proc. 48th Eur. Microw. Conf. (EuMC)*, Sep. 2018, pp. 946–949.

[21] H. Wang, M. Aust, K. Tan, and T. Trinh, "Monolithic Q band active array module and antenna," *Appl. Microw.*, vol. 5, no. 1, pp. 88–102, Winter 1993.

[22] A. R. Vilenskiy et al., "Co-design and validation approach for beam-steerable phased arrays of active antenna elements with integrated power amplifiers," *IEEE Trans. Antennas Propag.*, vol. 69, no. 11, pp. 7497–7507, Nov. 2021.

[23] W. Liao, A. R. Vilenskiy, R. Maaskant, T. Emanuelsson, V. Vassilev, and M. V. Ivashina, "MmWave metal bowtie slot array element integrating power amplifier MMIC via on-chip probe to enhance efficiency and bandwidth," *IEEE Trans. Antennas Propag.*, vol. 70, no. 9, pp. 8110–8121, Sep. 2022.

[24] W.-C. Liao et al., "A Ka-band active integrated antenna for 5G applications: Initial design flow," in *Proc. 2nd URSI Atlantic Radio Sci. Meeting (AT-RASC)*, 2018, pp. 1–4.

[25] G. Gonzalez, *Microwave Transistor Amplifiers Analysis and Design*. Upper Saddle River, NJ, USA: Prentice-Hall, 1996.

[26] K. Kurokawa, "Power waves and the scattering matrix," *IEEE Trans. Microw. Theory Techn.*, vol. MTT-13, no. 2, pp. 194–202, Mar. 1965.

[27] A. Niang, A. de Lustrac, G.-P. Piau, G. Sabanowski, and S. N. Burokur, "VHF antenna miniaturization using external non-foster matching circuit," *Microw. Opt. Technol. Lett.*, vol. 59, no. 4, pp. 986–991, Apr. 2017.

[28] M. Roberg and Z. Popovic, "Analysis of high-efficiency power amplifiers with arbitrary output harmonic terminations," *IEEE Trans. Microw. Theory Techn.*, vol. 59, no. 8, pp. 2037–2048, Aug. 2011.

[29] Y. Chung et al., "Effects of output harmonic termination on PAE and output power of AlGaN/GaN HEMT power amplifier," *IEEE Microw. Wireless Compon. Lett.*, vol. 12, no. 11, pp. 421–423, Nov. 2002.

[30] C. Craeye and D. González-Ovejero, "A review on array mutual coupling analysis," *Radio Sci.*, vol. 46, no. 2, pp. 1–25, Apr. 2011.

[31] I. Leito, L. Jalukse, and I. Helm, "Estimation of measurement uncertainty in chemical analysis (analytical chemistry) course," Univ. Tartu, Tartu, Estonia, 2018.